CHINA FOUNDRY Research & Development
Vol. 23 No. 1 January 2026
www.springer.com/41230
https://doi.org/10.1007/s41230-026-4234-2

Thermal simulation method for researching solidification process of ductile iron pipe based on heat transfer similarity of characteristic unit of ductile iron pipe

Gan-chao Zhai, Gong-ao Zhu, Shao-dong Hu, Bin Yang, Jie-yu Zhang, *Xiang-ru Chen, and **Qi-jie Zhai
Center for Advanced Solidification Technology, School of Materials Science and Engineering, Shanghai University, Shanghai 200444, China

Abstract: Centrifugal casting of ductile iron pipe is a high-temperature, semi-continuous production process. However, conducting laboratory research on the solidification process of centrifugal casting of ductile iron pipe presents significant challenges. In this study, a novel research method was introduced for investigating the solidification process of ductile iron pipe, namely thermal simulation of ductile iron pipe. Comparative research was conducted on the microstructure and properties of the thermal simulation sample and the ductile iron pipe. The findings indicate that the thermal simulation sample and ductile iron pipe exhibit good heat transfer similarity and microstructure similarity. The difference of cooling rate between thermal simulation sample and ductile pipe is less than 0.24 °C·s^{-1}, and the difference of microstructure content of free cementite, ferrite, and pearlite is less than 5%. The tensile strength of annealed ductile iron pipe is 466 MPa, with an elongation of 16.1% and a Brinell hardness of 156.5 HBW. In comparison, the tensile strength of annealed thermal simulation sample is 482.0 MPa, with an elongation of 15.5% and a Brinell hardness of 159.0 HBW. These results suggest that the thermal simulation experimental research method is both scientific and feasible, offering an objective, reliable, and cost-effective approach to laboratory research on ductile iron pipe.

Keywords: ductile iron pipe; centrifugal casting; thermal simulation; microstructure; mechanical property

CLC numbers: TG143.5 **Document code:** A **Article ID:** 1672-6421(2026)01-062-11

1 Introduction

Ductile iron pipe (DIP) has been widely used in the field of water supply and drainage network and heating pipelines owing to its high tensile strength, good elongation, strong corrosion resistance, ease of installation, long service life, good seismic performance, and minimal heat loss[1-9]. Currently, centrifugal casting is the predominant method for producing DIP[10,11], which is a high-temperature, opaque, semi-continuous, and large-scale production process. Furthermore, the phase transition process in the centrifugal casting of DIP is complex[12-15]. Consequently, conducting laboratory research on the solidification process of DIP presents significant challenges. Dissection of industrial test samples remains the most common and relevant research method. However, employing industrial tests for systematic research on DIP is not only costly and difficult to implement, but also poses challenges in ensuring data completeness and seriality. Furthermore, the resource consumption of systematic industrial test is huge and the experimental duration is extensive. Therefore, finding a laboratory method to investigate the solidification process of DIP holds great significance for advancing the production of high-performance and lightweight DIP.

The research methods for the solidification process of DIP include industrial test, numerical simulation, physical simulation, and thermal simulation. The application of numerical simulation to the solidification

*Xiang-ru Chen

Female, born in 1981, Ph. D. Her research interests mainly focus on analysis of composition and microstructure of microalloyed casting materials.

E-mail: chenxr@shu.edu.cn

**Qi-jie Zhai

Male, born in 1959, Ph. D., Professor. His research interests mainly focus on solidification structure and control of metals.

E-mail: qjzhai@shu.edu.cn

Received: 2024-10-28; Revised: 2025-05-11; Accepted: 2025-06-23

process of metals requires the setting and simplification of a large number of initial conditions, boundary conditions, and thermo-physical parameters[16-18]. Furthermore, the results of numerical simulations often require practical verification to enhance their reliability. Consequently, it is difficult to accurately predict the actual solidification microstructure by using numerical simulation techniques alone[15, 19-20]. Physical simulations, which include transparent material simulation[21-23], water simulation[24, 25], and low melting point metal simulation[26], offer advantages in observing solidification phenomena and elucidating mechanisms; however, they cannot directly reflect the phenomena and laws of the metal melts in the metallurgical solidification process. Conversely, the thermal simulation method[27-29] proposed by the research team of Zhai at Shanghai University directly utilized the target metal as the test material and conducted thermal simulation experimental research based on the similarity of temperature field. This approach can directly reflect the solidification process of metal, and is an objective, reliable, and low-cost research method.

The aim of the present study is to validate the scientific and feasible of the thermal simulation-based experimental method for DIP. Firstly, based on the principle of the characteristic-unit heat transfer similarity, a novel thermal simulation approach for experimentally investigating the centrifugal casting process of DIP was proposed. Subsequently, the DIP thermal simulation experimental device was designed and developed. The device was used to prepare thermal simulation samples (TSSs). Then, the heat transfer conditions and as-cast microstructure between TSS and DIP were compared and analyzed. Additionally, the microstructure and mechanical properties of TSS and DIP in their annealed states were further studied.

2 Thermal simulation process for DIP

2.1 Process and characteristics of centrifugal casting

Figure 1 illustrates a schematic diagram of the centrifugal casting process for DIP. Figure 1(a) shows the initial state prior to the commencement of centrifugal casting. At this juncture, the centrifugal casting machine approached the sector ladle, extending the flow channel into the interior of the centrifuge. Subsequently, the spheroidized molten iron passed through the tundish and was transferred into the sector ladle. Upon the initiation of centrifugal casting, the position of the stream inoculation device and the flow channel was fixed, with the sector ladle turning over at a constant speed. The molten iron then entered the flow channel through the stream inoculation device, flowing through the flow channel and rushing into the high-speed rotating metal pipe mold. The centrifugal casting machine subsequently moved along the track, distancing itself from the sector ladle, until the iron completely covered the metal pipe mold, completing the casting. The metal pipe mold and the molten iron were rapidly cooled by the cooling action of water on the metal pipe mold outer surface. Once the temperature of the DIP dipped below 800 °C, the pipe pulling pliers were inserted into the interior of the DIP to pull the DIP out of the mold.

To elucidate the cooling characteristics of the production process for DIP, the numerical simulation method was employed to simulate the cooling curves of different positions of the pipe wall. Referencing the design guidelines for water-cooled centrifugal casting machines[30], the cooling time of DIP with nominal diameter of 800 mm (DN800-DIP) was 90 s, with an inlet temperature of 35 °C and an outlet temperature of 70 °C

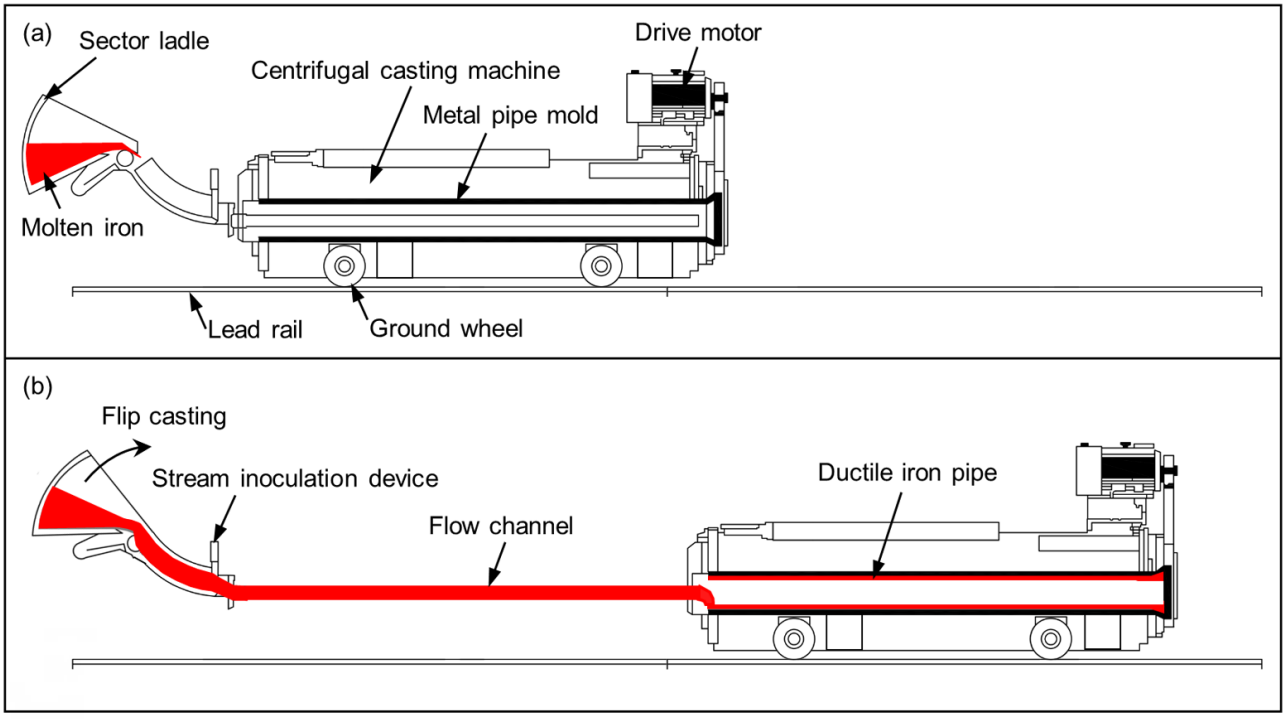

Fig. 1: Centrifugal casting process of DIP: (a) initial state of centrifugal casting; (b) end state of centrifugal casting

for the cooling water. Figure 2 presents the three-dimensional model of the metal pipe mold, sand mold, and DIP, which was meshed using ProCAST software. The metal pipe mold shaped the DIP's outer wall, while the sand mold shaped the DIP's inner socket. The ProCAST software was then utilized to simulate the cooling curves of the centrifugal casting process. During the simulation, the material of the DIP was EN-GJS-500-7, with a casting temperature set to 1,330 °C. The metal pipe mold material was 18CrMo4, with an initial temperature of 60 °C. The material of the sand mold was resin bonded sand, with an initial temperature of 50 °C. The thickness of the DIP and metal pipe mold was 11.7 mm and 9.8 mm, respectively, and the heat transfer coefficient between the DIP and the metal pipe mold was 1,800 $W \cdot m^{-2} \cdot K^{-1}$. The cooling condition of the outer surface of the metal pipe mold was water cooling, and the heat transfer coefficient between the metal pipe mold and the cooling water was 5,000 $W \cdot m^{-2} \cdot K^{-1}$. The cooling condition of the inner surface of the DIP was air cooling, and the heat transfer coefficient between the inner surface of the DIP and the air was 500 $W \cdot m^{-2} \cdot K^{-1}$. The heat transfer coefficients between the DIP and the metal pipe mold and the sand mold were both 500 $W \cdot m^{-2} \cdot K^{-1}$. Centrifugal casting process was used, the rotation speed of the metal pipe mold was 250 $r \cdot min^{-1}$. Figure 3 illustrates the simulated cooling curves of different positions within the DIP during the centrifugal casting process. The curves indicate a substantial difference in the radial cooling rates between the inner and rapid cooling side of the DIP during the cooling process.

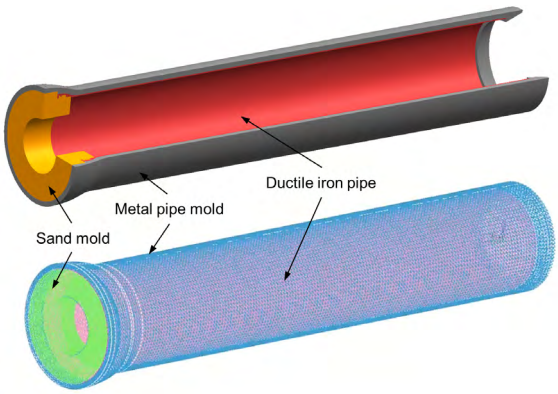

Fig. 2: Three-dimensional model and grid division diagram of metal pipe mold, sand mold, and DIP

2.2 Characteristics of as-cast DIP microstructure

Figure 4 illustrates the microstructure of the as-cast DIP. Figure 4(a) presents the graphite microstructure, observed consecutively from the slow cooling side to the rapid cooling side. The graphite structure of DIP mainly consists of spherical graphite, with only a small amount of aggregated spherical and vermicular graphite at the slow cooling side. Figure 4(e) depicts the matrix microstructure of the as-cast DIP, observed consecutively from the slow cooling side to the rapid cooling side. The matrix of slow cooling side comprises ferrite, pearlite, and cementite. The ferrite content gradually decreases from the slow cooling side to the rapid cooling side, while the pearlite content displays an initial increase followed by a subsequent decrease. In contrast, the cementite content increases progressively, with the matrix at the rapid cooling side primarily composed of pearlite and cementite. The cooling rate of the solidification process in metal mold centrifugal casting production of DIP is significantly rapid. The rapid cooling during casting produces a microstructure characterized by a significant presence of free cementite reaching 39.3%, which imparts cross-section with 'white mouth' characteristic, while the proportion of pearlite in the rapid cooling side is only 15.5% [Fig. 5(a)][32-34].

Figure 5 presents the quantitative results of the microstructure of as-cast DIP at the slow cooling side, middle position, and rapid cooling side. The slow cooling rate at the slow cooling side results in lower nodularity compared to that in the rapid cooling side. The nodularity of as-cast graphite increases from 82.9% at the slow cooling side to 88.2% at the rapid cooling side. Moreover, the graphite quantity is higher in the rapid cooling side than in the slow cooling side, exhibiting considerable variation across different size ranges. The number of spherical graphite particles in the size range of 1–5 μm is 534 mm^{-2} for the slow cooling side and 718 mm^{-2} for the rapid cooling side, while for the size range of 5–10 μm, the counts are 361 mm^{-2} and 481 mm^{-2}, respectively. The content of free cementite in the rapid cooling side is 39.3%, substantially higher than 6.2% found in the slow cooling side. The ferrite content decreases from 25.1% in the slow cooling side to 3.7% in the rapid cooling side, and the pearlite content also decreases from 47.8% to 15.5% as it transitions from the slow to rapid cooling side. The above statistical methods for microstructures are consistent with those in Section 3.

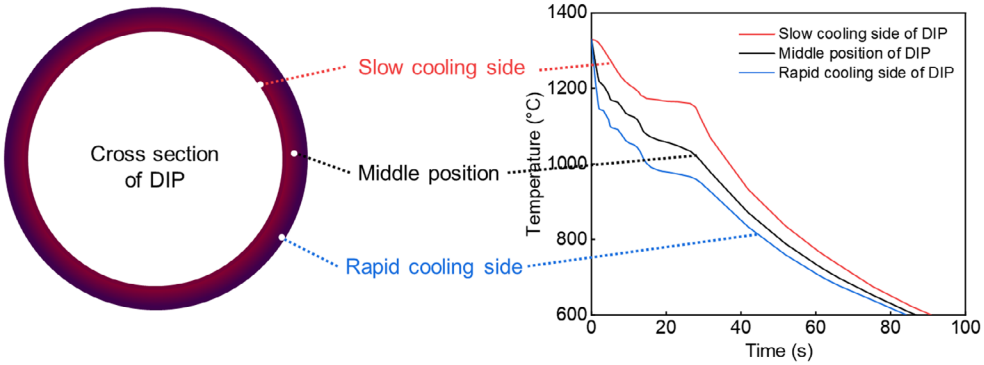

Fig. 3: Schematic diagram of cross section temperature field and cooling curves at different positions of DIP

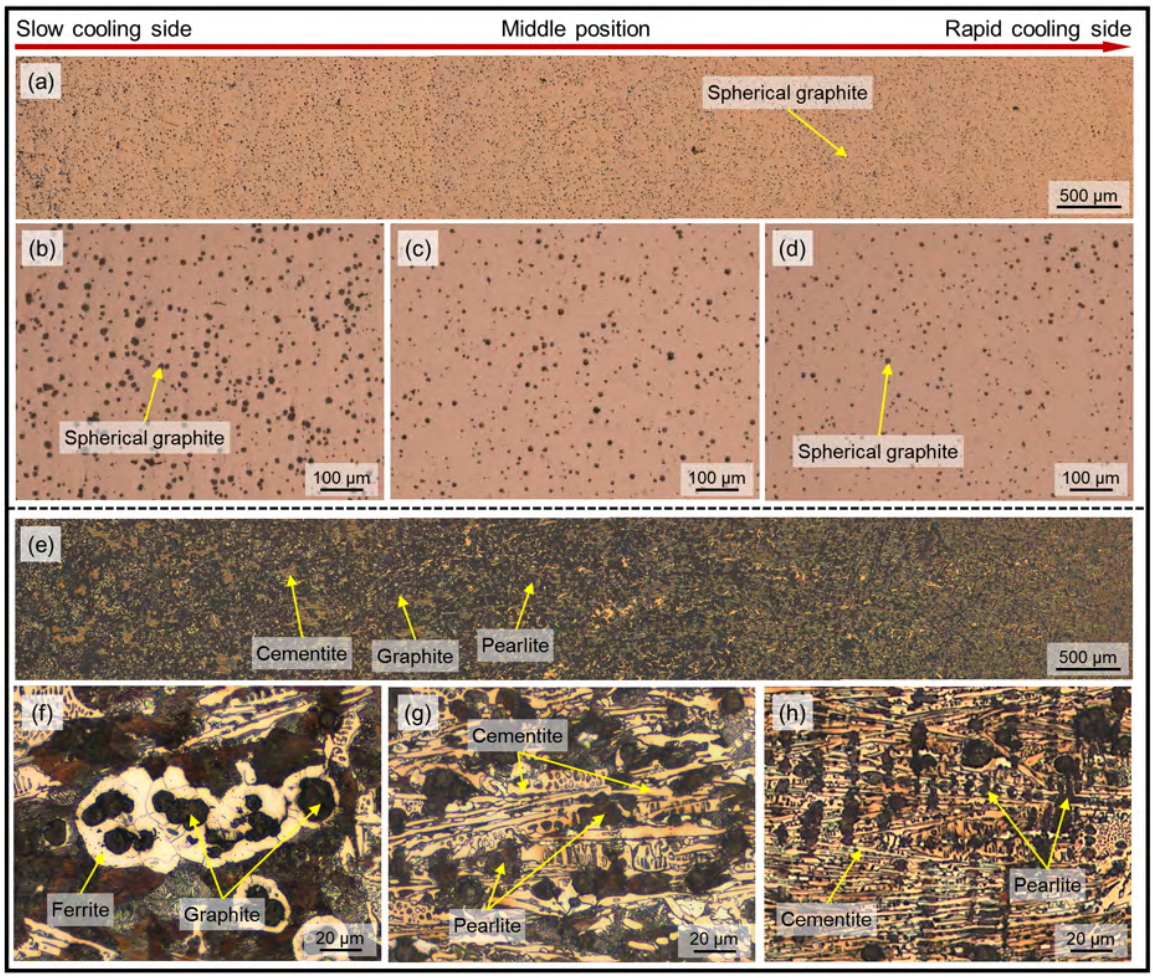

Fig. 4: Microstructure of as-cast DIP: (a) graphite microstructure from slow cooling side to rapid cooling side; (b, c, d) graphite microstructure of slow cooling side (b), middle position (c), and rapid cooling side (d); (e) matrix microstructure from slow-cooling side to rapid cooling side; (f, g, h) matrix microstructure of slow cooling side (f), middle position (g), and rapid cooling side (h)

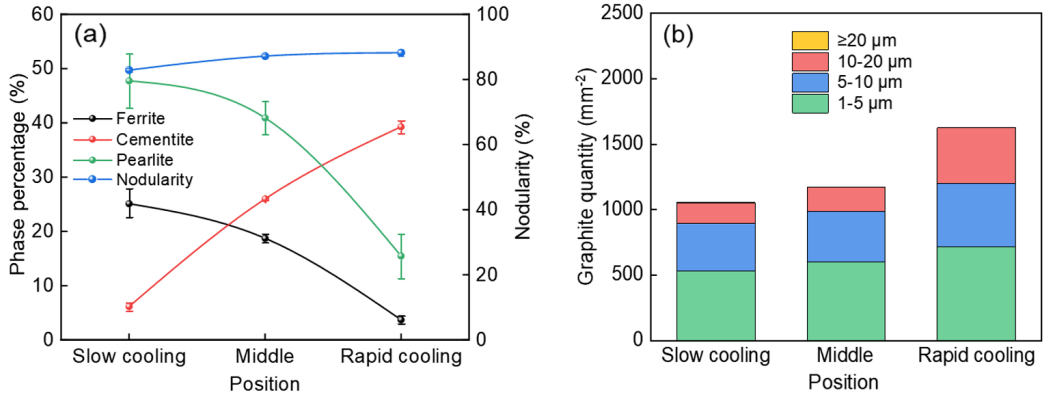

Fig. 5: Quantitative statistical results of microstructure of DIP: (a) quantity of graphite; (b) nodularity and phase content

2.3 Principle of thermal simulation-based experimental method

Currently, there are relatively few laboratory research methods for thin-walled fittings produced by centrifugal casting with large differences between internal and external cooling rates. Research team of Zhai[28, 34-37] has proposed an innovative method for thermal simulation of metal solidification process based on thermal similarity of characteristic units. This method reproduces offline the external conditions experienced by characteristic units solidified under metallurgical production circumstances, utilizing principles of thermal similarity and intelligent regulation. To ensure that the thermal simulation of the DIP accurately reflects the heat transfer conditions of the actual centrifugal casting process, it is crucial for the characteristic unit of the DIP to include a sample that extends radially from the slow cooling side to the rapid cooling side.

The ability of the DIP thermal simulation method in replicating the actual solidification process depends on its

accurate representation of the heat transfer characteristics of the DIP solidification. The analyses in Section 2.2 indicate that the heat transfer characteristics of the DIP solidification are marked by two key features: a rapid overall cooling rate and a radial cooling rate characterized by a gradient change.

Figure 6 presents the schematic diagram of the thermal simulation method for the DIP solidification process. According to the production process and gradient cooling rates, and microstructure of water-cooled metal mold centrifugal casting DIP [Figs. 6(a) and (b)], the thermal simulation device for DIP [Fig. 6(c)] was designed. Firstly, the numerical simulation of the solidification process for centrifugal DIP was conducted by using the centrifugal casting module in ProCAST (Fig. 2). Continuous cooling curves were obtained from various positions and the thermal simulation characteristic unit [Fig. 6(d)] was selected from the cross-section of the DIP. Subsequently, the cooling curves for the rapid cooling side, slow cooling side, and half wall thickness of the DIP [Fig. 6(e)] were selected to design the cooling condition simulator for DIP [Fig. 6(f)]. The thermal simulation characteristic unit of the DIP was put into the cooling condition simulator in the DIP thermal simulation device. The wall thickness of the cooling condition simulator was 12 mm, which closely approximated that of the DN800-DIP. The TSS cooling conditions were regulated by adjusting the materials and thicknesses of both the rapid cooling module and the slow cooling module in the cooling condition simulator, resulting in TSS that aligned with the solidification process of DIP. It is possible to modify the size and material of both the rapid cooling module and the slow cooling module, incorporating options such as gray cast iron, graphite chill, and furan resin sand, thereby enabling the simulation of various cooling conditions. In this study, the rapid cooling module was constructed from pure copper, while the slow cooling module was composed of furan resin sand. Furthermore, the solidification process with gradient cooling rate from the rapid cooling side to the slow cooling side was realized, and the as-cast microstructure with gradient change was obtained. Finally, the laboratory thermal simulation research of water-cooled metal mold centrifugal casting DIP was realized.

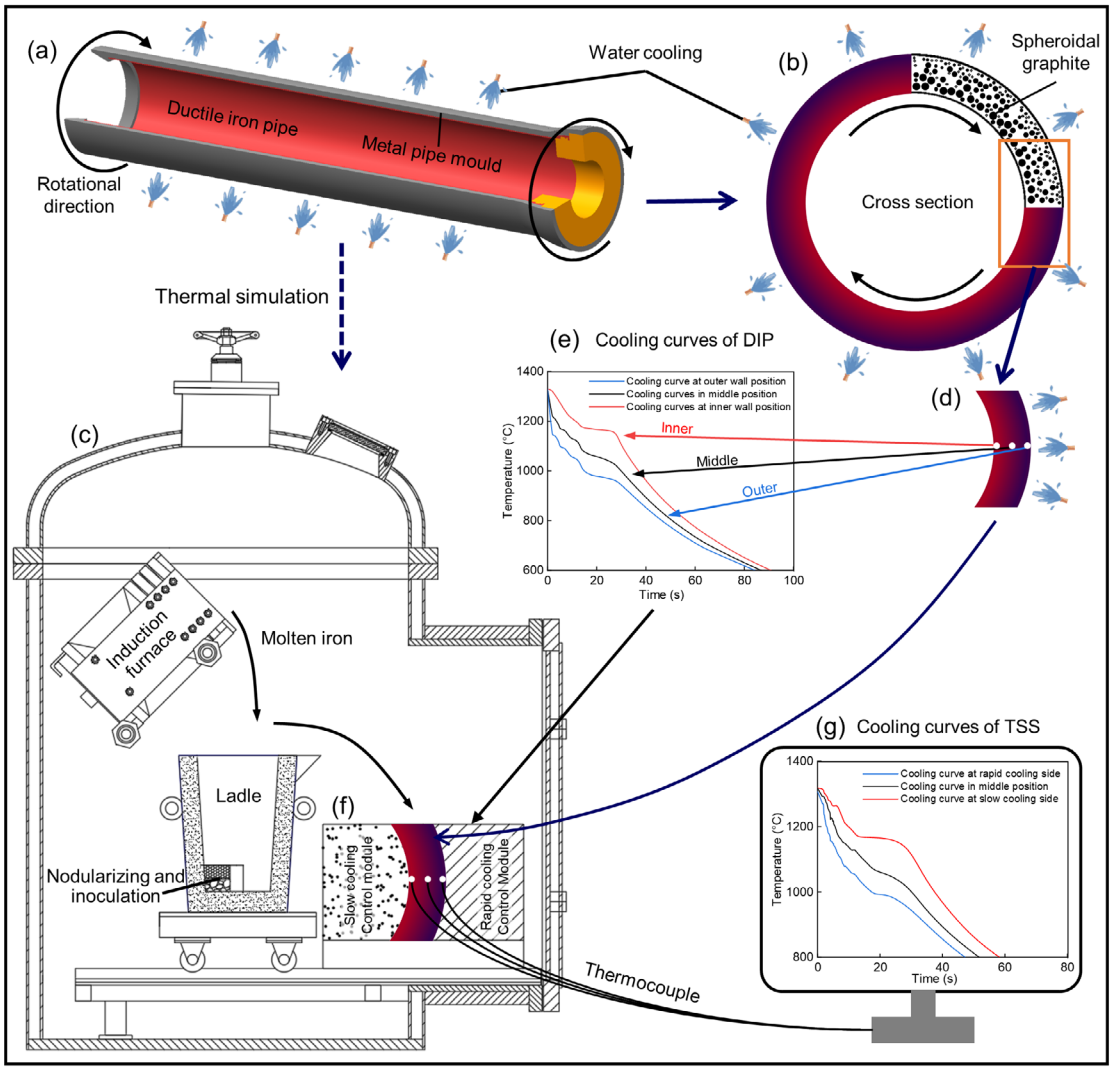

Fig. 6: Schematic diagram of thermal simulation method for DIP: (a) centrifugal casting machine; (b) enlarged cross section schematic diagram of DIP; (c) ductile iron pipe thermal simulation device; (d) DIP solidification characteristic unit, thickness is 11.7 mm; (e) cooling curves of ductile iron pipe at different positions; (f) cooling conditions simulator for DIP, thickness of TSS is 12 mm; (g) measured temperature curve

3 Materials and methods

The TSS was prepared using the DIP thermal simulation device. The raw materials for this experiment included high-quality Q10 pig iron, T7 low-carbon steel, ferrosilicon, and ferromanganese. The 14 kg medium frequency induction melting furnace was utilized to melt raw materials, where foundry pig iron, and carbon steel were completely melted at 1,480 °C. Following this, the ferrosilicon and ferromanganese alloys were added, and held at 1,480 °C for 10 min. Subsequently, deslagging agent was added, and the iron was transferred into the pouring ladle after slagging-off. Before pouring, 1.5wt.% of spheroidizing agent (FeSiMg8RE3), 0.8wt.% of inoculant (75SiFe), sheet iron, and an appropriate amount of deslagging agent were sequentially placed in the pit reaction chamber at the bottom of the ladle. Figure 7 illustrates the heat treatment process curve for the TSS. The annealing treatment comprised heating to a temperature range of 930–960 °C and holding for 15 min, followed by wind cooling to 750–800 °C at a cooling rate of approximately 0.6 °C·s^{-1}, and subsequently cooling within the furnace for 15 min to reduce the TSS temperature to 650–750 °C, and finally air cooling to room temperature.

Metallographic samples of 20 mm×12 mm×10 mm were prepared on the TSS, with the observation surface being ground and polished. The microstructure was observed using a ZEISS Axio-Image A2M metallographic microscope, and the graphite nodularity, roundness and quantity at the middle position were quantified using Image Pro Plus software. The matrix microstructure of the specimens was observed after corrosion with 4% nital for 6–10 s. The content of ferrite, pearlite, cementite, and graphite, as well as the grain size of ferrite in the annealed state, were measured at the middle position of each specimen. Among these parameters, the graphite nodularity, roundness, and content were evaluated according to GB/T 9441-2021, while the ferrite grain size was assessed based on GB/T 6394-2017.

Tensile test specimens measuring 70 mm in length and 5 mm in diameter were prepared in accordance with ISO 2531:2009

Table 1: Chemical compositions of DIP and TSS (wt.%)

	C	Si	Mn	P	S	Mg	Fe
DIP	3.53	2.25	0.21	0.03	0.006	0.038	Bal.
TSS	3.61	2.30	0.26	0.06	0.004	0.042	Bal.

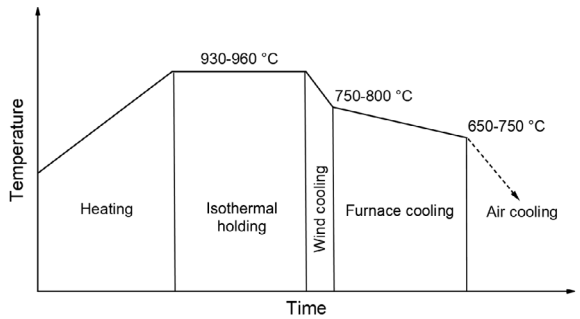

Fig. 7: Heat treatment process curve of TSS

(Fig. 8). The tensile tests were conducted on a Zwick 100 kN electronic material testing machine, with a crosshead separation rate of 4 mm·min^{-1}. Macro hardness was assessed in accordance with the GB/T 231.1-2018 standard, utilizing an HBS-3000 Brinell hardness tester. For the Brinell hardness test, a 2.5 mm diameter indenter was selected, and a test force of 1,839 N was applied, maintained at $F \cdot D^{-2}$=30 for a duration of 15 s.

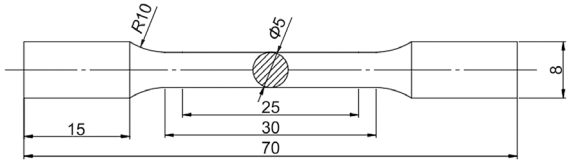

Fig. 8: Tensile test specimen size (unit: mm)

4 Results and discussion

4.1 Heat transfer conditions

During the cooling process of DIP in the metal pipe mold of the centrifugal casting machine, the heat is transferred from the molten iron to the mold from the DIP's rapid cooling side. Subsequently, this heat is taken away by the cooling water on the outer side of the metal pipe mold, which is similar to unidirectional, one-dimensional heat transfer. Generally, the average cooling rate was adopted to control the cooling process of DIP. The calculation method for the average cooling rate is illustrated in Eq. (1):

$$v = \frac{T_1 - T_2}{\Delta t} \quad (1)$$

where v is the average cooling rate of the cooling process, T_1 is the casting temperature, T_2 is the average temperature of the cast pipe at the time of pulling out, Δt is the time interval between the initial contact of molten iron with the metal pipe mold and the pulling out DIP after solidification.

Figure 9 presents a comparison of the cooling curves at different positions along the pipe wall for TSS and DIP. The average cooling rates for TSS and DIP were calculated using Eq. (1), and the results are listed in Table 2. The trends in cooling rates for both TSS and DIP are consistent, and the cooling rate from slow cooling side to rapid cooling side follows a monotonically increasing gradient change. A comparison of the results presented in Fig. 9 and Table 2 reveals that the difference in cooling rates between TSS and DIP, from the slow cooling side to the rapid cooling side, is less than 0.24 °C·s^{-1}. This indicates a good heat transfer similarity. Therefore, it can be concluded that the heat transfer conditions for TSS and DIP are similar.

4.2 As-cast microstructure

Figure 10 illustrates the comparison of the as-cast graphite microstructure between TSS and DIP. Both exhibit a consistent trend from the slow cooling side to the rapid cooling side: as the cooling rate increases, the quantity of graphite initially decreases and then increases. The graphite content decreases initially and then increases with rising cooling rate, while the nodularity slightly decreases and then increases. Overall, the

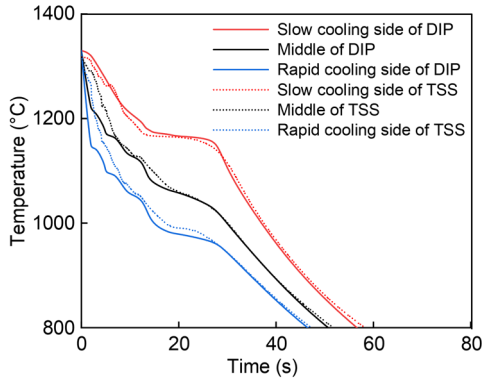

Fig. 9: Comparison of cooling curves between TSS and DIP

Table 2: Average cooling rate of TSS and DIP (°C·s^{-1})

Position	Slow cooling side	Middle	Rapid cooling side
DIP	9.39	10.80	11.46
TSS	9.15	10.58	11.30

change trend in the as-cast graphite microstructure is the same for both TSS and DIP.

Figures 11(a) and (b) illustrate the microstructure at different positions of DIP and TSS, respectively. The phase constitution and distribution of the microstructure of TSS, from the slow cooling side to the rapid cooling side, resemble those of DIP. The slow cooling side is characterized by the presence of pearlite, ferrite, and a small amount of free cementite. The middle position consists of pearlite, modified ledeburite, and a certain amount of free cementite. Conversely, the rapid cooling side consists of a large amount of free cementite, pearlite, and a small amount of ferrite. Figures 11(e), (f), and (g) show the quantitative results of the microstructure content at different positions of the TSS and DIP, showing a gradual increase in free cementite content alongside a decrease in ferrite and pearlite from the slow cooling side to the rapid cooling side. The free cementite content in TSS at different positions is slightly lower than that in DIP, with the lowest concentration observed on the slow cooling side of TSS at 3.26%. This observation indicates that the cooling rate of TSS is slightly lower than that of DIP. Additionally, the ferrite content of the TSS near the slow cooling side is marginally lower than that of DIP, which is opposite near the rapid cooling side. This discrepancy is attributed to the less effective cooling of the rapid cooling side of TSS compared to that of DIP. Furthermore, the pearlite content in TSS from the slow cooling side to the rapid cooling side is averaged at 3.8%, which is higher than that in DIP. This difference can be explained by the overall lower cooling rate of TSS relative to DIP, resulting in a slightly lower content of free cementite from the slow cooling side to the rapid cooling side of TSS, consequently leading to the transformation of the excess carbon element in TSS into pearlite.

In conclusion, the free cementite, ferrite, and pearlite contents exhibit only minor differences between TSS and DIP at different positions, with the difference not exceeding 5%. This finding indicates that the as-cast microstructures of TSS and DIP exhibit a good microstructure similarity.

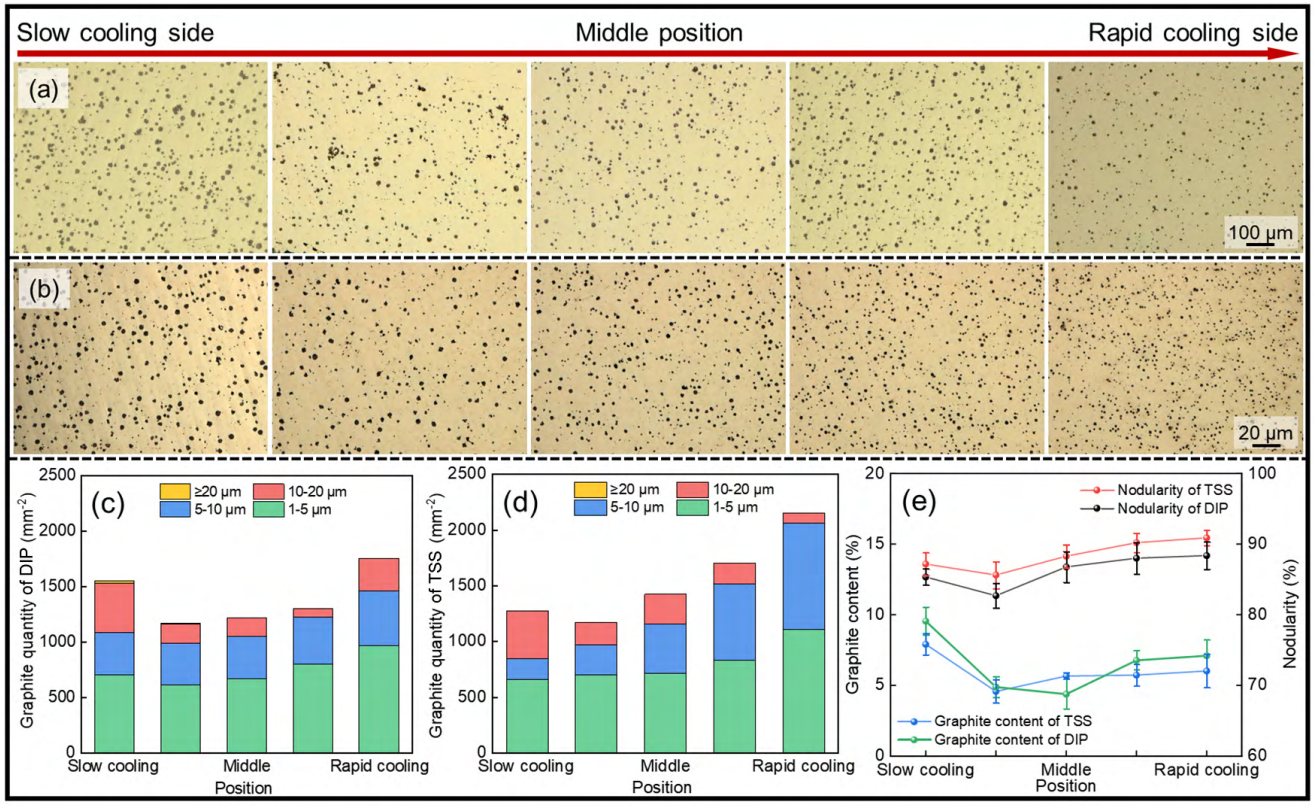

Fig. 10: Comparison of as-cast graphite microstructure between DIP and TSS: (a) graphite microstructure of DIP; (b) graphite microstructure of TSS; (c) graphite quantity of DIP; (d) graphite quantity of TSS; (e) graphite content and nodularity

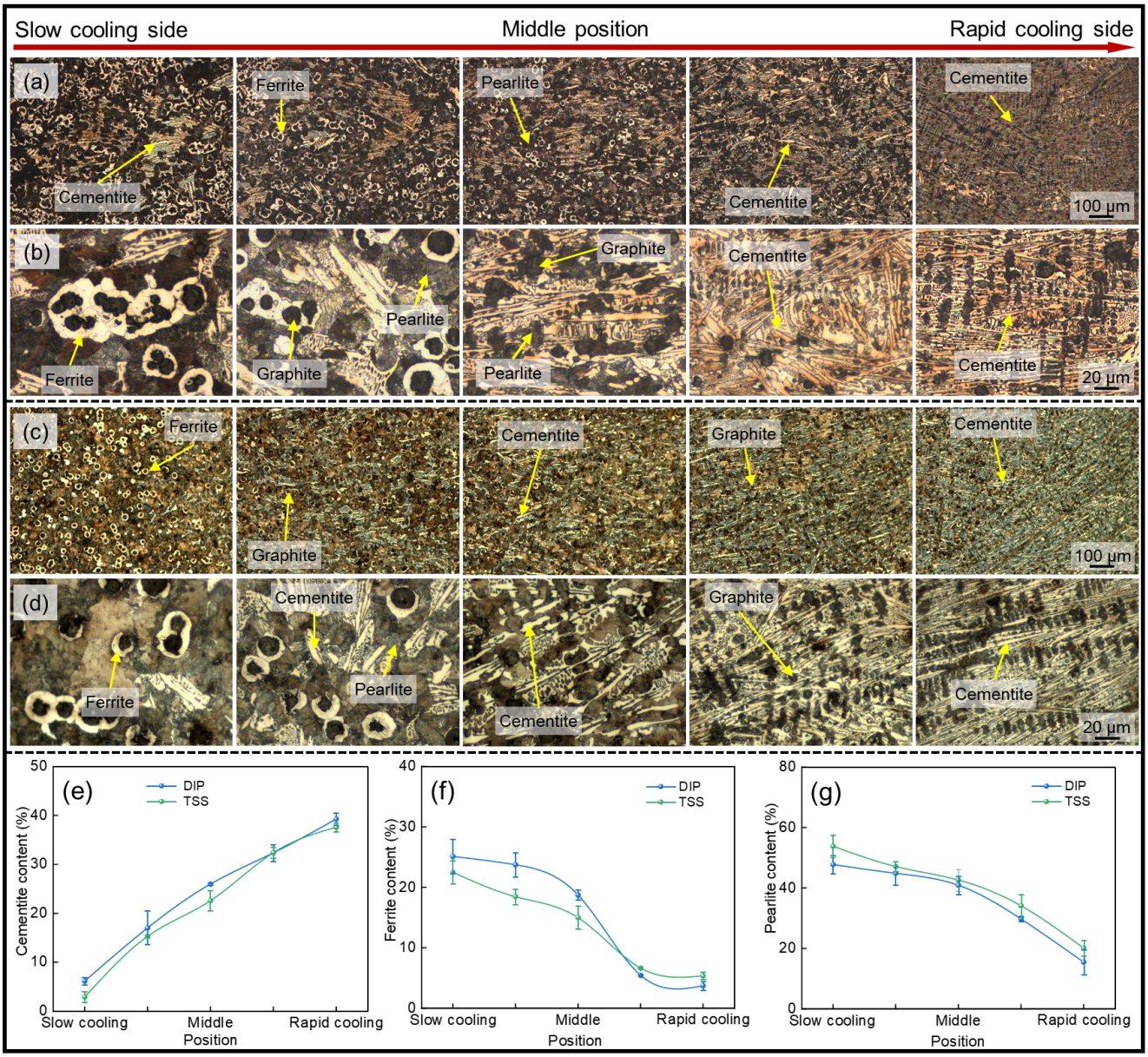

Fig. 11: Comparison of as-cast matrix microstructure between TSS and DIP: (a) matrix microstructure of DIP from slow cooling to rapid cooling side; (b) high magnification picture of matrix microstructure of DIP; (c) matrix microstructure of TSS from slow cooling to rapid cooling side; (d) high magnification picture of matrix microstructure of TSS; (e) free cementite content; (f) ferrite content; (g) pearlite content

4.3 Heat treatment microstructure

Figure 12 illustrates the microstructure of DIP and TSS in annealed states. After annealing treatment, the free cementite and pearlite in the microstructure of DIP and TSS are basically eliminated, and the matrix microstructure is ferrite. Figures 12(e), (f), and (g) present quantitative analyses of microstructure content at different positions in DIP and TSS, revealing a progressive increase in the ferrite content and a corresponding decrease in free cementite and pearlite content from the slow cooling side to the rapid cooling side. Among them, the free cementite and pearlite contents decrease at a slower rate in the middle position, and even shows a slight upward trend. The free cementite content at different positions in TSS is slightly lower than that in DIP, indicating that the cooling rate of the TSS is marginally lower than the actual cooling rate of DIP. Moreover, the ferrite content in TSS is approximately 3.8% (average value) higher than that in DIP at the rapid cooling side. The overall cooling rate of TSS is lower than that of DIP, resulting in a slightly lower free cementite content of TSS from the slow cooling side to the rapid cooling side than that of DIP. Specifically, the cooling rates in TSS are lower than those in DIP: by 0.24 $°C·s^{-1}$ at the slow cooling side, 0.22 $°C·s^{-1}$ in the middle position, and 0.16 $°C·s^{-1}$ at the rapid cooling side (as shown in Table 2).

4.4 Mechanical properties

Figure 13 illustrates the tensile property curves for both DIP and TSS, indicating that TSS not only able to resemble DIP in microstructure, but also possesses mechanical properties comparable to those of DIP. Table 3 presents the mechanical

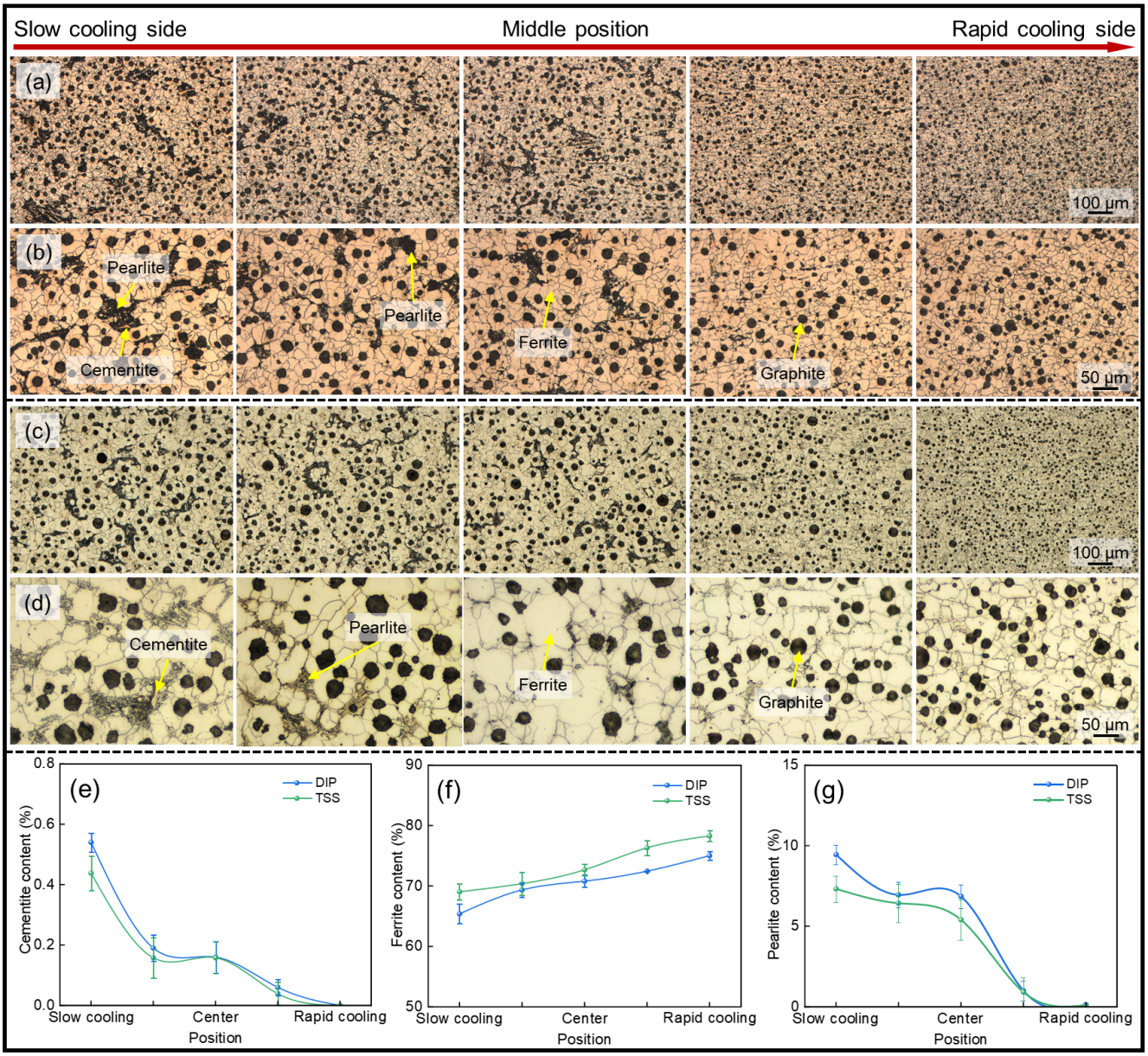

Fig. 12: Comparison of annealed matrix microstructure between TSS and DIP: (a) matrix microstructure of DIP from slow cooling to rapid cooling side; (b) high magnification picture of matrix microstructure of DIP; (c) matrix microstructure of TSS from slow cooling to rapid cooling side; (d) high magnification picture of matrix microstructure of TSS; (e) free cementite content; (f) ferrite content; (g) pearlite content

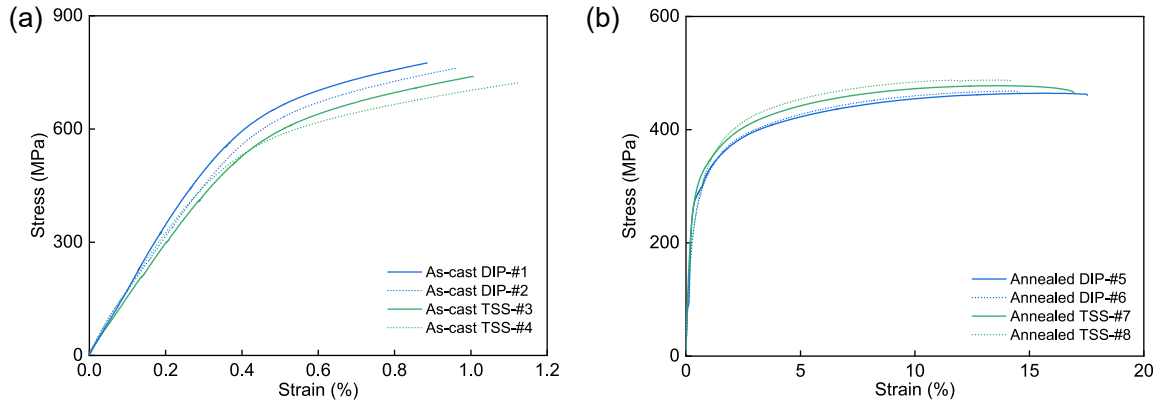

Fig. 13: Mechanical properties of DIP and TSS: (a) mechanical properties of as-cast; (b) mechanical properties of annealed state

Table 3: Mechanical properties of DIP and TSS

	Number	Tensile strength (MPa)	Average (MPa)	Elongation (%)	Average (%)	Brinell hardness (HBW)	Average (HBW)
As-cast DIP	#1	775	763.5	0.89	0.95	418	415.0
	#2	761		1.00		412	
As-cast TSS	#3	739	744.0	1.00	1.06	381	384.5
	#4	723		1.13		388	
Annealed DIP	#5	464	466.0	17.5	16.10	156	156.5
	#6	468		14.6		157	
Annealed TSS	#7	477	482.0	16.9	15.50	160	159.0
	#8	487		14.1		158	

properties of DIP and TSS. As-cast DIP exhibits an average tensile strength of 763.5 MPa, an elongation of 0.95%, and an average Brinell hardness of 415.0 HBW. In comparison, as-cast TSS displays an average tensile strength of 744.0 MPa, an elongation of 1.06%, and an average Brinell hardness of 384.5 HBW. The lower cementite content in as-cast TSS compared to DIP accounts for its reduced tensile strength and Brinell hardness. Following the annealing treatment, the tensile strength and Brinell hardness of DIP decrease to 466.0 MPa and 156.5 HBW, respectively, while the elongation increases to 16.10%. In its annealed state, TSS shows an average tensile strength of 482.0 MPa, an elongation of 15.50 %, and an average Brinell hardness of 159.0 HBW.

5 Conclusions

(1) The centrifugal casting process of DIP is characterized by rapid overall cooling rate, radial cooling gradient, and significant discrepancy of cooling rate between slow and rapid cooling sides. Based on the heat transfer characteristics of the cooling process of DIP, a thermal simulation device for the solidification process of DIP has been designed and developed. The heat transfer condition of DIP solidification can be reproduced offline by using the heat simulation method based-on characteristic-unit heat transfer similarity.

(2) The difference of cooling rate between TSS and DIP does not exceed 0.24 $°C·s^{-1}$, indicating that the TSS is similar to the centrifugal casting process of DIP in terms of heat transfer conditions.

(3) Although there are differences in the microstructure constituents at different locations between the TSS and DIP, the differences in free cementite, ferrite, and pearlite contents between TSS and DIP do not exceed 5%. This observation suggests that the as-cast microstructure of TSS and DIP exhibits a good microstructure similarity.

(4) The tensile strength of annealed DIP is measured at 466 MPa, with an elongation of 16.1%. In contrast, the tensile strength of annealed TSS is measured at 482 MPa, with an elongation of 15.5%. These results indicate that TSS not only exhibits microstructural similarities to DIP, but also demonstrates mechanical properties consistent with those of DIP.

(5) Thermal simulation-based experimental method for DIP proposed in this study is both scientific and feasible. Additionally, it offers an objective, reliable, and low-cost experimental method for the industrial production of DIP.

Acknowledgment

This work was financially supported by the National Natural Science Foundation of China (52130109).

Conflict of interest

Prof. Qi-jie Zhai is an EBM of *CHINA FOUNDRY*. He was not involved in the peer-review or handling of the manuscript. The authors have no other competing interests to disclose.

References

[1] Jones L J N, Kong D, Tan B T, et al. Water pipes in Malaysia: Technical and capital cost comparison. In: Proceeding of the 6th International Conference of Accounting, Business, and Economics (ICABEC 2020), Terengganu, Malaysia, 2021: 41.
[2] Yang H C, Chang C Y, Liu G Y, et al. Effect of support condition on the mechanical behavior of ductile iron pipes buried at shallow depth within the backfill of controlled low strength material. Transportation Geotechnics, 2023, 41: 101016.
[3] Mitra S, Roy D, Bhattacharyya T. Effect of boron on the manufacturing process and final properties of ductile iron pipes (DI pipes). Ironmaking & Steelmaking, 2018, 45(1): 1–5.
[4] Chang Z P, Zhao Q, Lu H J. Optimal selection of pipe material for a high-head long-distance water transmission pipeline based on the fuzzy analytic hierarchy process. Journal of Pipeline Systems Engineering and Practice, 2025, 16(2): 04024074
[5] Primin O. The efficiency of using ductile iron water pipes in soft soil. E3S Web of Conferences, 2023, 419: 01012.

[6] He X Z, Yam M C H, Zhou Z Y, et al. Inhomogeneity in mechanical properties of ductile iron pipes: A comprehensive analysis. Engineering Failure Analysis, 2024, 163: 108459.
[7] Yan X F, Deng C Y, Zhao Y H, et al. Mechanical performance study of pipe-liner composite structure based on the digital image correlation method. IEEE Transactions on Instrumentation and Measurement, 2023, 72: 1–12.
[8] Jibreen A M. Investigation of models to predict the remaining useful life of prestressed concrete cylinder pipe. Doctoral Dissertation, America: The University of Texas at Arlington, 2022: 7–10.
[9] Blount J. How to identify cast iron and ductile iron pipe. Indianapolis: 2022 American Society of Civil Engineers, 2022: 219–226.
[10] Thacker K, Joshi H, Patel N J. Analysis and optimization of parameters for casting ductile iron pipes. International Journal of Engineering Research and General Science, 2015, 3(3): 403–429.
[11] Yang H C, Chang C Y, Liu G Y, et al. Effect of support condition on the mechanical behavior of ductile iron pipes buried at shallow depth within the backfill of controlled low strength material. Transportation Geotechnics, 2023, 41: 101016.
[12] Guo X J, Stefanescu D M. Solid phase transformation in ductile iron. Transactions of the American Foundrymen's Society, 1997, 105(6): 533–543.
[13] Zhang B M. Current situation and prospect of casting pipe industry. Modern Cast Iron, 2002, (1): 1–4. (In Chinese)
[14] Liu J H, Yan J S, Zhao X B, et al. Precipitation and evolution of nodular graphite during solidification process of ductile iron. China Foundry, 2020, 17(4): 260–271.
[15] Liu L C, Cao Y L, Ma C S, et al. Coupling simulation and mechanism analysis of grain formation and growth in horizontal centrifugal casting. International Journal of Metalcasting, 2024: 1–13.
[16] Wang X X, Chen R R, Wang Q, et al. Influence of rotation speed and filling time on centrifugal casting through numerical simulation. International Journal of Metalcasting, 2023, 17(2): 1326–1339.
[17] Wang Y J, Qin F C, Qi H P, et al. Interfacial bonding behavior and mechanical properties of a bimetallic ring blank subjected to centrifugal casting process. Journal of Materials Engineering and Performance, 2022, 31(4): 3249–3261.
[18] Liu L C, Ma C S, Cao Y L, et al. Filling and solidification behavior simulation of manufacturing DC53 cutter ring tube through centrifugal casting process. Metallurgical and Materials Transactions: B, 2025, 56(2): 2009–2019.
[19] Mohapatra S, Sarangi H, Mohanty U K. Effect of processing factors on the characteristics of centrifugal casting. Manufacturing Review, 2020, 7: 26.
[20] Gawronska E, Dyja R. 3D simulations of solidification with liquid phase flow. In: IOP Conference Series: Materials Science and Engineering, 2020, 776(1): 012029.
[21] Jackson K A, Hunt J D. Transparent compounds that freeze like metals. Acta Metallurgica, 1965, 13(11): 1212–1215.
[22] Zhong H G, Zhang Y H, Chen X R, et al. In situ observation of crystal rain and its effect on columnar to equiaxed transition. Metals, 2016, 6(11): 271–271.
[23] Huang W D, Wang L L. Solidification researches using transparent model materials–A review. Science China Technological Sciences, 2012, 55(2): 377–386.
[24] Tao P, Shao H, Ji Z J, et al. Numerical simulation for the investment casting process of a large-size titanium alloy thin-wall casing. Progress in Natural Science: Materials International, 2018, 28(4): 520–528.
[25] Keerthiprasad K S, Murali M S, Mukunda P G, et al. Numerical simulation and cold modeling experiments on centrifugal casting. Metallurgical and Materials Transactions: B, 2011, 42(1): 144–155.
[26] Timmel K, Eckert S, Gerbeth G, et al. Experimental modeling of the continuous casting process of steel using low melting point metal alloys-the LIMMCAST program. ISIJ International, 2010, 50(8): 1134–1141.
[27] Chen X R, Zhong H G, Song C J, et al. Effect of forced convection on grain refinement of S32205 duplex stainless steel. In: International Conference on Advanced Materials and Engineering Materials, Qingdao China, 2013, 683: 626–630.
[28] Li Z J, Chen X R, Ao L, et al. Effect of melt superheat on structure of unsteady state unidirectionally solidified duplex stainless steel. Materials Science and Technology, 2014, 27(4): 818–822.
[29] Zhong H G, Chen X R, Han Q Y, et al. A thermal simulation method for solidification process of steel slab in continuous casting. Metallurgical and Materials Transactions: B, 2016, 47(5): 2963–2970.
[30] Zhang B M. Centrifugal casting. Beijing: China Machine Press, 2004: 157. (In Chinese)
[31] Meng W, Lei Y L, Wang X, et al. Interface characteristics and mechanical properties of wire-arc depositing Inconel 625 superalloy on ductile cast iron. Surface & Coatings Technology, 2022, 440: 128493.
[32] Zhang Y, Chen R R, Wang Q, et al. Examining the role of rare earth elements on grey iron's microstructural and mechanical properties. International Journal of Cast Metals Research, 2024, 37(2): 117–124.
[33] Sun D, Zhang L F, Xiong Y, et al. Research on cost-effective new alloy cast iron. In: 5th Annual International Workshop on Materials Science and Engineering, 2019, 585(1): 012025.
[34] Zhong H G, Wang R J, Zhai Q J. Experimental research methods and applications of solidification processes in metallurgical industry. Iron & Steel, 2022, 57(10): 11. (In Chinese)
[35] Zhai Q J, Zhong H G, Chen X R, et al. Thermal simulation technology and equipment of continuous casting solidification process based on characteristic element. China Metallurgy, 2021, 31(8): 134–134. (In Chinese)
[36] Li R X, Gao Y L, Liang J P, et al. Physical simulation method and device for solidification tissue growth of continuous casting billet. China, CN200710042685.6, May 2nd, Intellectual Property Publishing House Co., Ltd., 2012. (In Chinese)
[37] Yuan H Z, Zhong H G, Zhai Q J. Thermal simulation technique for solidification process of continuous casting and its application. The Chinese Journal of Process Engineering, 2022, 22(10): 1400–1413. (In Chinese)